AGU100 ADVANCING EARTH AND SPACE SCIENCE

JGR

Journal of Geophysical Research: Oceans

RESEARCH ARTICLE

10.1002/2017JC013693

Special Section:

Sea State and Boundary Layer Physics of the Emerging Arctic Ocean

Key Points:

- Images from drifting buoys provide the first in situ quantification of sea ice floe growth processes
- Lateral floe growth is limited by stress induced by the wave field
- Observed floe behavior agrees with theoretical models and informs model parameter choices

Supporting Information:

- Supporting Information S1
- Movie S1
- Movie S2

Correspondence to:

L. Roach,
Lettie.Roach@niwa.co.nz

Citation:

Roach, L. A., Smith, M. M., & Dean, S. M. (2018). Quantifying growth of pancake sea ice floes using images from drifting buoys. *Journal of Geophysical Research: Oceans*, *123*. https://doi.org/10.1002/2017JC013693

Received 13 DEC 2017
Accepted 28 FEB 2018
Accepted article online 26 MAR 2018

Quantifying Growth of Pancake Sea Ice Floes Using Images From Drifting Buoys

Lettie A. Roach[1,2], Madison M. Smith[3], and Samuel M. Dean[1]

[1]National Climate Centre, National Institute of Water and Atmospheric Research, Wellington, New Zealand, [2]School of Geography, Environment and Earth Sciences, Victoria University of Wellington, Wellington, New Zealand, [3]Applied Physics Lab, University of Washington, Seattle, WA, USA

Abstract New sea ice in the polar regions often begins as small pancake floes in autumn and winter that grow laterally and weld together into larger floes. However, conditions in polar oceans during freezeup are harsh, rendering in situ observations of small-scale sea ice growth processes difficult and infrequent. Here we apply image processing techniques to images obtained by drifting wave buoys (SWIFTs) deployed in the autumn Arctic Ocean to quantify these processes in situ for the first time. Small pancake ice floes were observed to form and grow gradually in freezing, low-wave conditions. We find that pancake floe diameters are limited by the wave field, such that floe diameter is proportional to wavelength and amplitude over time. Floe welding correlates well with sea ice concentration, and the observations can be used to estimate a key model parameter for floe size evolution. There is some agreement between observed lateral growth rates and those predicted using a theoretical model based on heat flux balance, but the model lateral growth rates are too conservative in these conditions. These results will be used to inform description of lateral floe growth and floe welding in new models that evolve sea ice floe size distribution.

Plain Language Summary Sea ice, which is frozen seawater, can take many different forms depending on its surrounding conditions. If the ocean is still, it might form as large, thin sheets of sea ice. If there are waves on the ocean surface, sea ice forms as "pancake" floes—small circular pieces of ice. There are very few close-up observations of sea ice made during freezing conditions, and even less where waves are present such that pancake floes form. This is partly due to the challenge of completing a field campaign in the cold and dark of winter, as well as the limited number of platforms capable of making observations in thin, new ice. Here we present an analysis of images captured by buoys that drift with the ice in the Arctic during freezeup. These images show how pancake floes evolve over time as a result of wave and freezing conditions. We compare observations to what different theoretical models would predict for the observed conditions. These comparisons can be used to inform the development of new large-scale models for sea ice evolution, which is important for polar climate.

1. Introduction

Formation of sea ice in the polar regions is strongly coupled to the ocean and atmosphere. When the upper ocean layer is at or slightly below the freezing point, small frazil crystals begin to form. Sheets of sea ice can form under two different pathways, depending on the wind and wave conditions. In quiescent conditions, frazil crystals freeze together to form nilas, thin sheet ice that is initially transparent. Nilas then grows in thickness by congelation growth on the underside of the ice. In more dynamic conditions with wind and wave forcing, semiconsolidated frazil slush can oscillate and form near-circular floes with upturned edges called pancakes (Weeks & Ackley, 1986). These may grow laterally, by further adfreezing of frazil crystals (Wadhams et al., 1987). When pancakes remain in contact for sufficient periods of time, they may freeze together (Shen & Ackley, 1991). The final step in this sequence is the transition from loosely joined pancakes to a complete sheet of joined, or cemented, pancakes (Weeks & Ackley, 1986). Sea ice resulting from pancake growth is likely to be rougher than that resulting from nilas growth, thus impacting oceanic and atmospheric fluxes. Pancake sea ice formation is common in the Antarctic (Wadhams et al., 1987) and is becoming more common in the increasingly ice-free Arctic (Jones, 2009) where new ice growth is subject to more active wave fields (Thomson & Rogers, 2014).

However, large-scale sea ice models, such as those used in global climate models, typically describe only sea ice growth by formation of nilas. For example, the state-of-the-art sea ice models CICE5 and LIM3 form some new volume of sea ice from flux balance and preferentially set the new ice to have a low thickness covering a large surface area (Hunke et al., 2015; Vancoppenolle et al., 2009). Like CICE5 and LIM3, most sea ice components of global climate models employ a probability distribution in sea ice thickness in order to calculate thermodynamic and dynamic sea ice evolution (Hunke et al., 2010). They do not include information on sea ice floe size, which means they are currently unable to represent sea ice growth by formation of pancakes.

Recent work by Horvat and Tziperman (2015, 2017), Zhang et al. (2015), Bennetts et al. (2017), and Zhang et al. (2016) has, however, laid the foundations for the inclusion of a sea ice floe size distribution, either defined in parallel or coupled to the ice thickness distribution, in current sea ice models. Including a floe size distribution would allow a fuller description of physical processes such as lateral melt, dynamic floe collisions and floe fracture, as well as lateral growth. These processes are either not currently included in models (lateral growth and floe fracture) or heavily parametrized (lateral melt and floe collisions—see e.g., Hunke et al., 2015). Several models (e.g., CICE, Hunke et al., 2015) include parametrizations for lateral melt based on observational studies. For example, a functional form for a lateral melt rate was found in laboratory work by Josberger and Martin (1981), which was fit to data obtained in the Arctic by Maykut and Perovich (1987), and is used in models today.

Fewer empirical results exist for sea ice growth processes than for melt processes, largely due to the inaccessibility of polar regions during winter. Recent model studies show that observational constraints on sea ice freezing processes are required. In the context of simulated floe size distributions, Horvat and Tziperman (2015) presented a scheme for lateral growth of sea ice floes, where the growth rate was computed by a geometrical partitioning of the ocean freezing potential. They do not cite any observational justification for this.

Neither Bennetts et al. (2017) nor Zhang et al. (2016) include lateral growth, but they both identify a separate growth process referred to as floe bonding (Bennetts et al., 2017) or floe welding (Zhang et al., 2016). This is the transition from loosely joined pancakes to cemented pancakes mentioned above, which is a freezing-together of floes, rather than a dynamic process, impacting only the floe size distribution and not sea ice concentration. Zhang et al. (2016) notes that the coalescence of sea ice floes is “difficult to determine” because of “lack of knowledge about the welding processes.” As there are no empirical observations justifying the appropriate rate of welding, Bennetts et al. (2017) represent welding processes by doubling their representative floe diameter (up to a maximum diameter) each time step in grid cells where the ocean temperature is below freezing. Similarly, Zhang et al. (2016) move all floes into the largest floe size category when the ice growth rate in a certain grid cell exceeds a certain threshold, a number which is chosen as part of their model tuning.

Roach et al. (2018b) include both lateral growth and floe welding. The welding scheme proposed uses the geometric probability of sea ice floes touching during freezing conditions, where the coefficient of proportionality is the rate of welding participation. A key aim of the present study is to constrain this welding rate constant.

While some field studies exist on the transition from frazil to pancake ice (Doble, 2009) and the kinematics of a pancake ice field (Doble & Wadhams, 2006; Rottier, 1992), to our knowledge there are no published field measurements of lateral floe growth or rates of floe welding. Using a one-dimensional model, Shen and Ackley (1991) showed that wave action can initiate and maintain collisions between floes on the order of seconds and suggest that floes can freeze together if this time scale is long enough, as observed in the field. We do not know of any laboratory observations of such floe welding interactions. Lateral growth of pancake sea ice has been measured in laboratory wave-ice flumes (Leonard et al., 1998; Onstott et al., 1998; Shen & Ackley, 1995; Shen et al., 2004), providing estimates of pancake formation on the time scale of hours to days. Shen et al. (2004) theorized that the ultimate diameter of pancake ice will be limited by tensile stress induced by the wave field. They found good correlation between observed maximum floe diameter and the observed tensile stress mode, with additional dependence on temperature and salinity, in a cold water tank. Results from laboratory experiments may not hold under different environmental conditions (Shen & Ackley, 1995) and do not always scale correctly to the real world (Doble, 2009), requiring validation by field observations.

The aim of the present study is to quantify the rate at which pancake sea ice floes grow laterally and weld together, processes that have been identified as important for sea ice model development. Pancake sea ice growth processes are observed in situ using time lapse images of the ocean surface in the autumn Arctic Ocean. A supervised image processing algorithm, described in section 3, is used to determine floe sizes and welding events. We describe the evolution of floe size and environmental conditions and quantify errors associated with image processing in section 4. In sections 5–7, we compare observations to predictions by three theoretical models, which describe different processes that would all be required to fully model evolution of sea ice floe size during freezing conditions. The three models describe the limiting diameter of pancake ice arising from stress induced by the wave field (Shen et al., 2004), evolution of the floe size distribution due to welding (Roach et al., 2018b), and evolution of the floe size distribution due to lateral growth (Horvat & Tziperman, 2015). The first of these has been validated by laboratory experiments. The latter two are used to evolve the floe size distribution in models and have not been constrained empirically. The observational analysis presented here evaluates these models to determine how atmospheric conditions and waves affect growth of pancake ice. These results are useful for future sea ice model development.

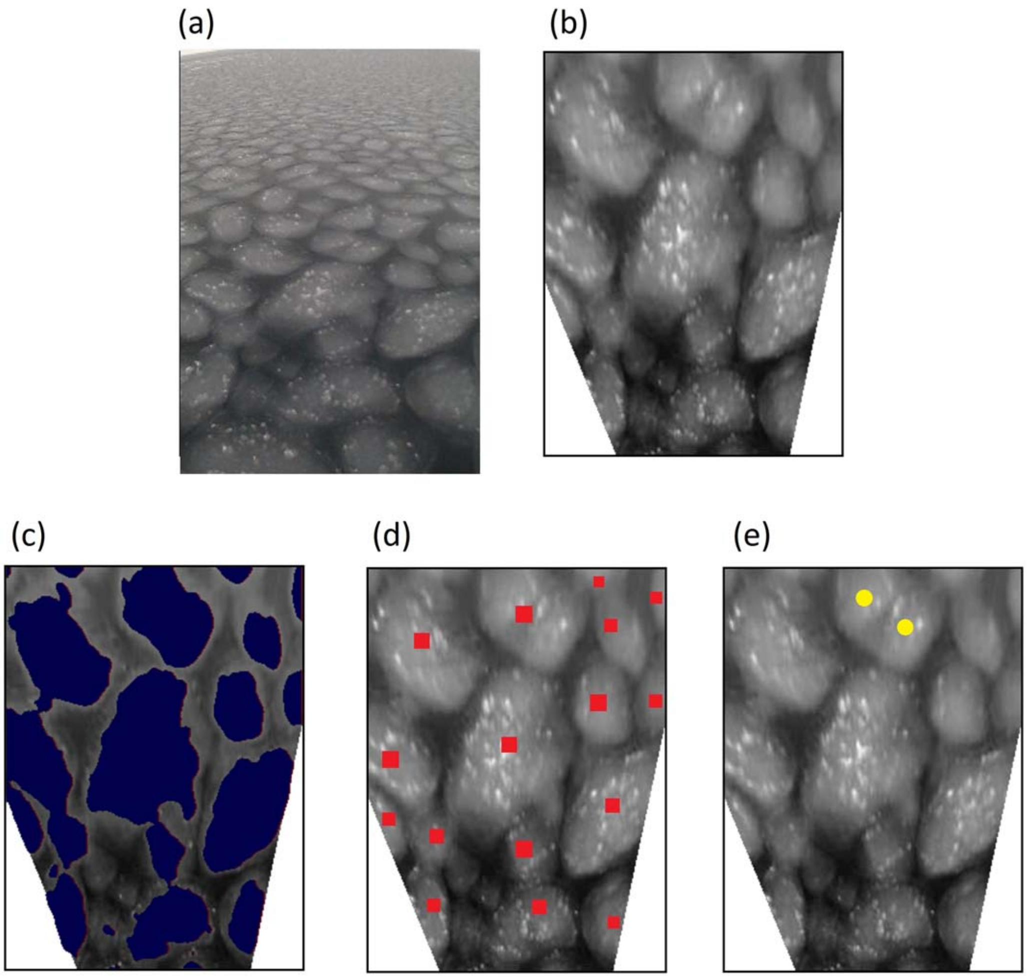

Figure 1. An example SWIFT image (a) as captured, (b) orthorectified, (c) with the area estimate from a fixed threshold (blue shading), (d) with the discrete floes found by a user-specified threshold (red squares), and (e) with the floe components found by a user-specified threshold, which split one discrete floe from Figure 1d into two floe components (yellow circles).

2. Data

The images used in this study were captured by SWIFT buoys (Surface Wave Instrument Floats with Tracking), which are free drifting systems designed to measure ocean waves, winds and near-surface turbulence (Thomson, 2012). SWIFTs are also equipped with serial cameras (4-D systems uCam) mounted on a mast 1 m above the water surface, which capture images of their surroundings in five bursts each hour. Raw (unorthorectified) images have a resolution of 320 $\times$ 240 pixels. The bursts are approximately 8 min long, recording 102 images at a frequency of 0.25 Hz, with the next 4 min allocated to processing data. An example image is shown in Figure 1a.

Wave spectra are determined from measurements of orbital velocity components (Herbers et al., 2012), made using a Microstrain 3DM-GX3-35 combination GPS receiver and Inertial Motion Unit (IMU), at a frequency of 4 Hz. GPS horizontal velocities have a resolution of 5 cm/s, which is sufficient to resolve most wave orbital motions (Thomson, 2012). Bulk wave parameters are calculated from the wave spectra following the standard formulations as defined in Herbers et al. (2012). Significant wave height, H_s, is calculated as $H_s=4\sqrt{m_0}$, where m_0 is the first moment of the spectrum. The energy-weighted period, T_e, is $T_e=\frac{m_0}{\sum Ef}$, where E and f are the energy and frequency respectively. Typical errors associated with H_s and T_e estimates are less than a few percent (Herbers et al., 2012). Water temperature and salinity 0.5 m below the surface are measured with an AADI Aanderaa Conductivity Sensor 4319. Air temperature is measured using an ultrasonic anemometer (Airmar PB200) 1 m above the surface, with a resolution of 0.1°C. More details on the platform can be found in Thomson (2012).

Two SWIFTs were deployed at approximately 72°29′N 158°41′W from the *R/V Sikuliaq* 26–27 October 2015, during the Sea State cruise in the Beaufort Sea region of the Arctic Ocean. Maps of SWIFT buoy deployment and recovery locations relative to sea ice area and land are shown in Figure 2. More details on the cruise and the context of these measurements can be found in Thomson et al. (2018). The buoys were left to drift for two days under freezing conditions and relatively low sea state. They buoys remained within 1 km of each other over the course of the deployment period. As confirmed by observers onboard the ship, the buoys were initially surrounded by open water, that froze, forming small pancake floes whose size increased over time. The evolution of the floe sizes in time can be seen in the videos provided as supporting information Movies S1 and S2.

While buoys were drifting, shipboard measurements were being made in the surrounding area. Of primary interest to this study are atmospheric flux measurements, estimated from a suite of instruments installed on the ship's mast, estimates of water temperature made from a towed thermistor ("Sea Snake"), and sea ice thicknesses made from hourly dip net samples.

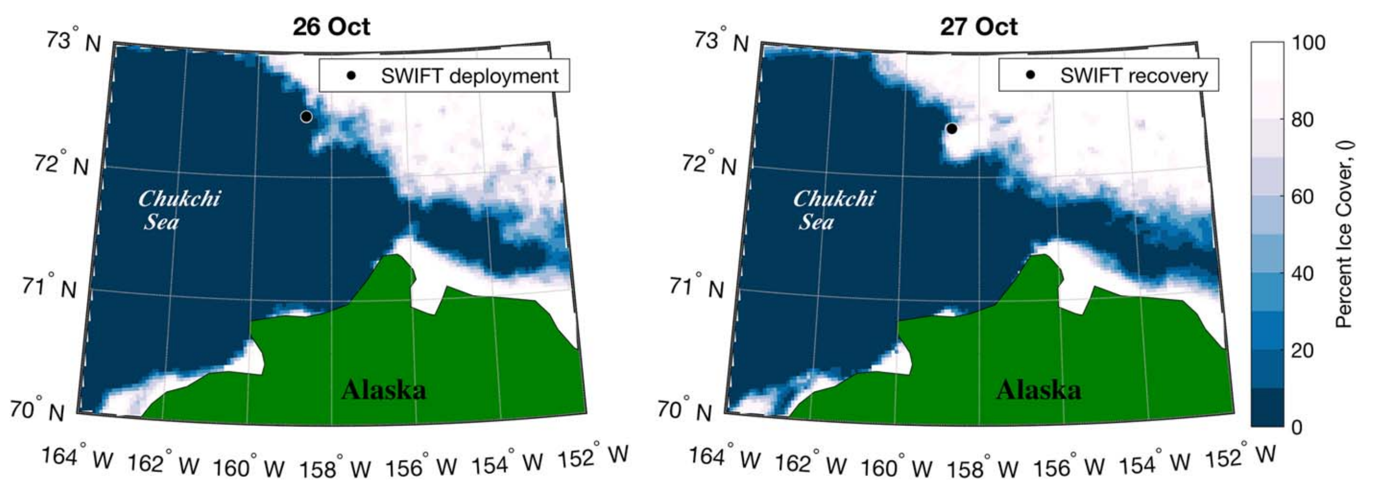

Figure 2. Maps showing sea ice coverage in area of SWIFT observations. SWIFT deployment and recovery locations (black points) are shown in context of ice concentration and extent from daily AMSR2 sea ice product (Spreen et al., 2008) from (left) October 26 and (right) October 27. Note that SWIFT 09 and 14 deployment and recovery locations are within 1 km, such that both can be represented by one point.

Net atmospheric fluxes, Q_{net}, were determined using shipboard turbulent flux measurements as

$$Q_{net}=Q_{si}-Q_{so}+Q_{li}-Q_{lo}-LHF-SHF. \quad (1)$$

Q_{si} is incoming (downwelling) shortwave radiation, Q_{so} is outgoing (upwelling) shortwave radiation, Q_{li} is incoming (downwelling) longwave radiation, Q_{lo} is outgoing (upwelling) longwave radiation, *LHF* is latent heat flux, and *SHF* is sensible heat flux. Details of the specific measurement methods and calculations can be found in Persson (2012) and Persson et al. (2002). The estimate of net atmospheric flux (Q_{net}) has an accuracy of 10 W/m^2.

The dip net is used to retrieve between three and six individual pancake ice samples over the side of the ship which are then manually measured (Wadhams et al., 2018). Ice thickness estimates are determined as an average of the observed thicknesses.

3. Methods

Images captured by the SWIFTs are processed using a series of standard image processing techniques in order to calculate (i) a rate of floe welding events and (ii) a lateral floe growth rate. The key methodological approach that allows us to separate these two concurrent processes is use of three levels of image brightness thresholding. First, images are processed to obtain estimates of sea ice area; second, to obtain estimates of the number of discrete sea ice floes; third, to obtain estimates of the number of floe “components” that, together, make up welded floes. In this latter step, we search within each discrete floe to see if brightness thresholding will further isolate any floe components within composite floes.

Quantifying growth of sea ice floes from these images requires that the drift of SWIFT buoys is Lagrangian with respect to the drift of sea ice. Lund, et al. (2018) show that SWIFTs drift with the surrounding ice, so we can assume that we are observing the same ice through time in a statistical sense, even though the sequence of images does not capture the exact same floes due to the random motion of the floes in and out of the camera frame. We further assume that each burst is representative of the ice conditions in that 12 min window. We sample ten images within each burst, selected at random, and then average each set of ten calculated ice properties in time. Naturally, since the images were taken in dynamic conditions, floes will touch and move apart. The choice of time averaging was designed to average out these temporary floe interactions.

Each selected image is undistorted based on intrinsic camera parameters using the *undistortImage* function in Matlab’s image processing toolbox, and orthorectified using the *imwarp* function, where the transformation object is determined by fitting a geometric transform to calibration images. This results in a bird’s eye view of the image in real-world coordinates (Figure 1b), where 1 pixel in the image corresponds to 4.6 mm in real-world coordinates.

Orthorectification assumes pitch and roll are zero such that the ocean surface is always oriented the same relative to the camera. Although pitch and roll values are recorded by the IMU in the SWIFT buoys, the IMU is not synchronized with image acquisition and thus cannot be used for orthorectification. Instead, average pitch and roll values recorded by the SWIFTs for each data burst are used to calculate the associated error in area that would result at the far edge of the orthorectified image, where the largest error due to buoy motion occurs.

Due to the small scale of the images, the differences in pixel intensity over ice and water are fairly uniform—apart from a front-to-back luminosity gradient—meaning that only simple image processing techniques are required. Color information is removed and the linear front-to-back luminosity gradient is corrected. We then apply simple image processing functions from the Open Source Computer Vision Library (OpenCV; Itseez, 2015). A bilateral filter removes noise from the image, while keeping the edges sharp, by applying Gaussian filters as function of space and as a function of pixel intensity. Next, fixed-level brightness thresholds are applied to binarize the image. We trialled the watershed algorithm, a geometric approach commonly used in floe size studies (e.g., Arntsen et al., 2015), but we found that this erroneously separated the rather long, oblong-shaped floes that appeared in some images. Therefore, only brightness thresholding is used to analyze the images here.

10.1002/2017JC013693

Visually, a single fixed threshold (97) gave a good separation of solid ice and water, from which the total ice area, $\mathcal{A}$, and concentration, C, were calculated (Figure 1c). This thresholding excludes the loose frazil crystals on floe edges. Frazil aggregations—which are very young pancakes where crystals have begun to freeze together but may not yet be completely consolidated—are included as solid ice. Other properties were calculated from each image by varying the fixed threshold to a value determined by eye. After thresholding, the OpenCV function for identifying contours in a binary image, retrieving only the extreme outer contours, can be used to count floes. Besides the total ice area, the key properties required for the analysis are the number of discrete floes, N_d, and the number of floe components, N_c, which includes all components of composite floes as well as noncomposite floes. If there are no welded or composite floes then $N_c = N_d$. If there is at least one welded or composite floe, $N_c > N_d$.

First, a fixed threshold is found that gives an accurate number of discrete floes, N_d (Figure 1d). Then a second fixed threshold is applied within each contour identified in the first step to calculate the number of floe components, N_c, within discrete floes (Figure 1e). The user thus decides whether floes are temporarily touching or welded together. As we expected there to be some subjectivity to this process, the algorithm was run twice by two different users. Comparing results from both trials gives some estimate of the error arising from the human component of the image analysis.

The initiation of each step is automated so that the user can run the code, produce figures, and adjust sliders to select thresholds where floe welding is included or ignored. If the user cannot find a threshold which returns an accurate number of floes, the user discards the image and it is replaced with another in that burst. In some bursts, it is not possible to find thresholds which give realistic numbers of floes; these bursts are ignored.

We define a representative floe area, for both the number of discrete floes (N_d) and the number of all floe components (N_c), $\bar{A}_d$ ($\bar{A}_c$) by assuming that all floes in an image have the same size, so $\bar{A}_d = \mathcal{A}/N_d$ ($\bar{A}_c = \mathcal{A}/N_c$). We choose this representative floe area as a metric because there is not much variation of floe size within each image: on average 80% of floe areas are within one order of magnitude of the mean. Equivalent radii, r, or diameters, $2r$, are calculated using $A = 4 \cdot 0.66 r^2$ (Rothrock & Thorndike, 1984), which accounts for noncircularity of floes.

Floe welding will increase the representative floe area because the total number of floes decreases, without changing the total ice area. Lateral floe growth will increase the total ice area as individual floes increase in area, without changing the total number of floes. Thus, the time rate of change of the representative area of discrete floes, $\bar{A}_d$, describes the evolution of floe size under both floe welding and lateral growth, while the time rate of change of the representative area of floe components, $\bar{A}_c$, describes evolution of floe size under lateral growth only. The separation of these two processes in the analysis requires conservation of ice area during floe welding. It is possible that the welding of two floes traps and consolidates loose frazil crystals in between them, thus violating conservation of total ice area, but we are unable to confirm this without more advanced image processing methods.

We include floes which are cut off by the image boundary, although this may cause a low bias in the average floe area. Excluding them would greatly reduce our sample size. Accuracy in absolute area values is not of primary importance as our analysis principally concerns growth rates or relative area values. When varying thresholds to identify contours in the image, it was noted that the algorithm may erroneously identify small specks as discrete objects. These appear to be points of high reflection from the ocean or crystals caused by orientation of the surface. To eliminate this effect, any individual floe areas which are less than 3% of the representative floe area are discarded in post-processing. This step impacts the floe counts (N_c and N_d) and individual floe areas.

The areas of individual discrete floes and floe components within each image are also calculated, but the algorithm performed more poorly here and so these are only used once in our analysis (to calculate the floe size distribution to compare to a theoretical lateral growth model in section 7). The individual areas are calculated from the thresholds used to count discrete floes and floe components (e.g., Figures 1d and 1e, respectively). To account for the lower accuracy of floe area estimates, individual areas are subsequently corrected by a normalization to the total ice area estimate obtained from the initial threshold (e.g., Figure 1c), $\mathcal{A}$, i.e.,

$$A_c^n = A_c^n \frac{\mathcal{A}}{\sum_n A_c^n}, \tag{2}$$

where n denotes individual areas. Thus, underestimated individual floe areas are increased in proportion to their size such that they sum to the total ice area $\mathcal{A}$.

Journal of Geophysical Research: Oceans 10.1002/2017JC013693

We proceed by describing how floes evolve in the study time period with environmental conditions, and then compare observational results to three models which describe floe size in sections 5–7.

4. Floe Size Evolution

Figure 3 shows the representative area of discrete floes and the representative area of floe components over the deployment period. The range of values observed is similar for both SWIFTs, and both show generally increasing areas, with some variability. The time variability, between results from the ten images from each 12 min burst (shaded region in Figure 3) is nonnegligible but does not obscure the overall behavior. The time variability is likely to be mostly due to floe motion; in the sequence of images, floes are observed to move in and out of the frame supporting information Movies S1 and S2.

We find that time variability is larger than error in area estimates arising from image processing, due to both subjectivity and wave motion. The two trials by different users show strong agreement (Figure 3), with a Pearson correlation coefficient of 99% for identification of discrete floes and 96% for identification of floe components. Time variability (shaded regions in Figure 3) exceeds the difference between the two user trials for all image bursts except one from SWIFT09 (which occurs at approximately 01:12). This strengthens confidence that the human component in estimates of floe areas and lateral growth rates is negligible, and we will henceforth show only the midpoint of the two trials. Errors due to pitch and roll range from upward of 20% at the beginning of the period to around 2% toward the end of the period, and are shown as error bars in Figure 3. We find that the error due to pitch and roll is relatively small, and smaller than the subburst time variability except at the very start of the SWIFT14 deployment.

Focusing on overall behavior, by using only the average values from the 10 images sampled in each 12 min window, Figure 4 shows evolution of representative floe area. The grey shading shows the contribution of lateral floe growth, computed from the representative area of floe components. The residual growth is the impact of floe welding on the representative floe area, which is much smaller than lateral growth.

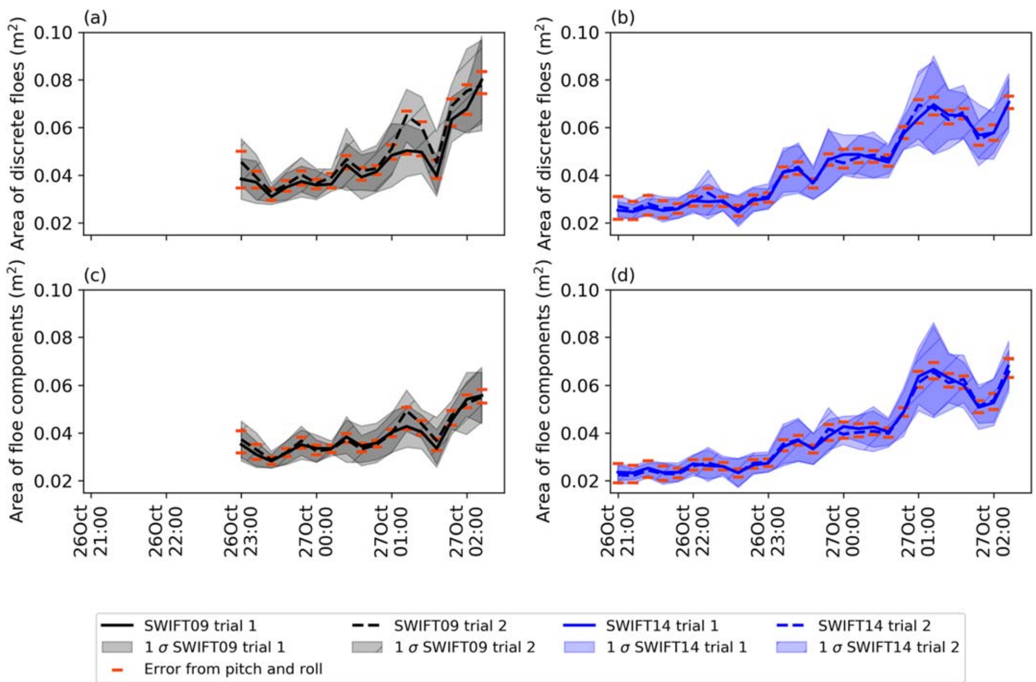

Figure 3. Burst-averaged floe areas over the deployment period where (a, b) show the representative area of discrete floes, and (c, d) show the representative area of floe components. Solid and dashed lines represent algorithm results from two different users. Shaded areas indicate ±one standard deviation in time for each burst, with the solid shaded region corresponding to the solid line, the dashed shaded region corresponding to the dashed line, and the darker shaded region corresponding to the overlap between the two standard deviation envelopes. Error bars (orange) show the error arising from assuming that pitch and roll are zero.

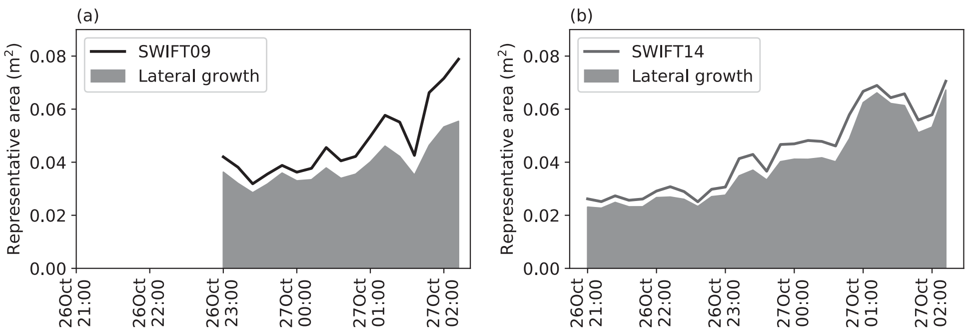

Figure 4. Evolution of burst-averaged representative areas of discrete floes, where the grey shading shows the contribution of lateral growth for (a) SWIFT09 and (b) SWIFT14.

Overall, we see a steady lateral growth throughout the deployment, of larger magnitude in SWIFT14 than SWIFT09. Welding area growth estimates are approximately constant in time from SWIFT14, but accelerate toward the end of the deployment period for SWIFT09. These differences between the ice evolution observed by the two SWIFTs may arise from slightly different environmental conditions. Generally the two SWIFTs observe similar floe size evolution, as we would expect based on their proximity. The representative areas from the two SWIFTs correlate well over the period where results are available from both, with a Pearson correlation coefficient of 0.66 for discrete floes and 0.70 for floe components (both $p < 1\%$).

Atmospheric and ocean variables measured continuously from the ship, including net atmospheric heat flux, sea surface temperature, and ice thickness, are not measured by SWIFT buoys and provide context for observations of ice growth. As the ship was often at long distance away from the buoys during the deployment period, we only use measurements from the ship when within 10 km of the buoy locations (Figure 5). The net atmospheric flux measured from the ship over the period was strongly negative, from the ocean to the atmosphere, ranging between -200 and -170 W/m^2. Sea surface temperatures measured from the ship dropped over the first few hours of ice growth from approximately $-0.8°$ to nearly $-1.4°$C. Average ice thickness, as estimated from dip net samples measured on the ship in two different locations, was 1.1 cm at 22:00 on 26 October and 4.2 cm 3.5 h later. These estimates are averages from six and three samples with standard deviation of 0.12 and 0.29 cm, respectively.

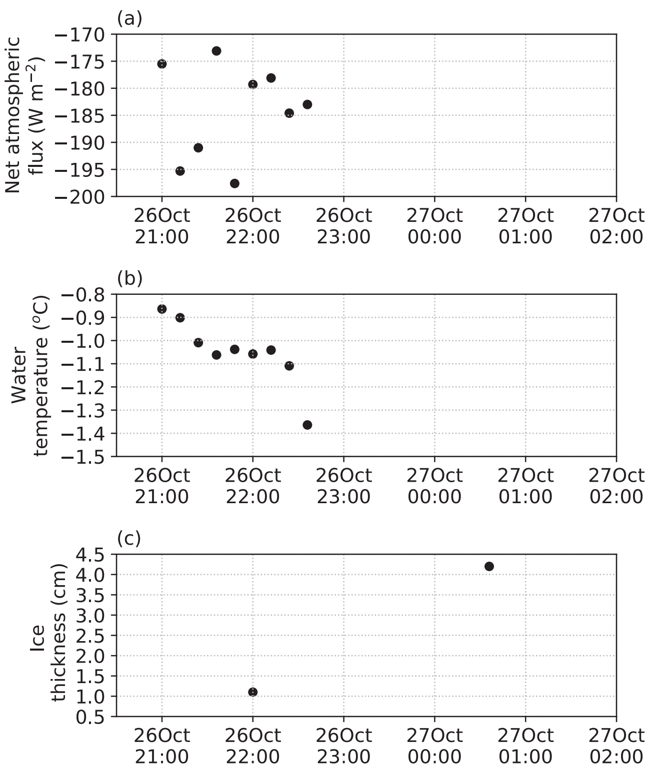

Figure 5. (a) Net atmospheric heat fluxes (Q_{net}), (b) sea surface temperature, and (c) ice thickness measured from the ship within 10 km of buoy locations.

Figure 6 shows representative areas of floe components together with air temperature at a height of 1 m and significant wave height recorded by each of the buoys. There are strong negative correlations between the representative area of floe components and air temperature (Pearson correlation coefficients -0.71 for SWIFT09 and -0.96 for SWIFT14, both $p < 1\%$), with floes increasing in size as the air temperature cools (Figures 6a and 6b). Correlations between the representative area and the water temperature 0.5 m below the surface were weaker. Water temperatures from this depth, which are above its freezing point, may not be a good indicator of mechanisms at the surface, which is subject to much colder conditions. A significant decrease in wave height was recorded by the SWIFTs during the deployment period (Figures 6c and 6d). Lateral growth is strongly negatively correlated to significant wave height for both buoys (Pearson correlation coefficients -0.71 for SWIFT09 and -0.90 for SWIFT14, both $p < 1\%$). Lead/lag analysis (not shown) provided some indication that significant wave height had a causative relationship with floe area but this was not conclusive.

There is also some correspondence between floe welding and significant wave height (Figure 7). For each image, the difference between

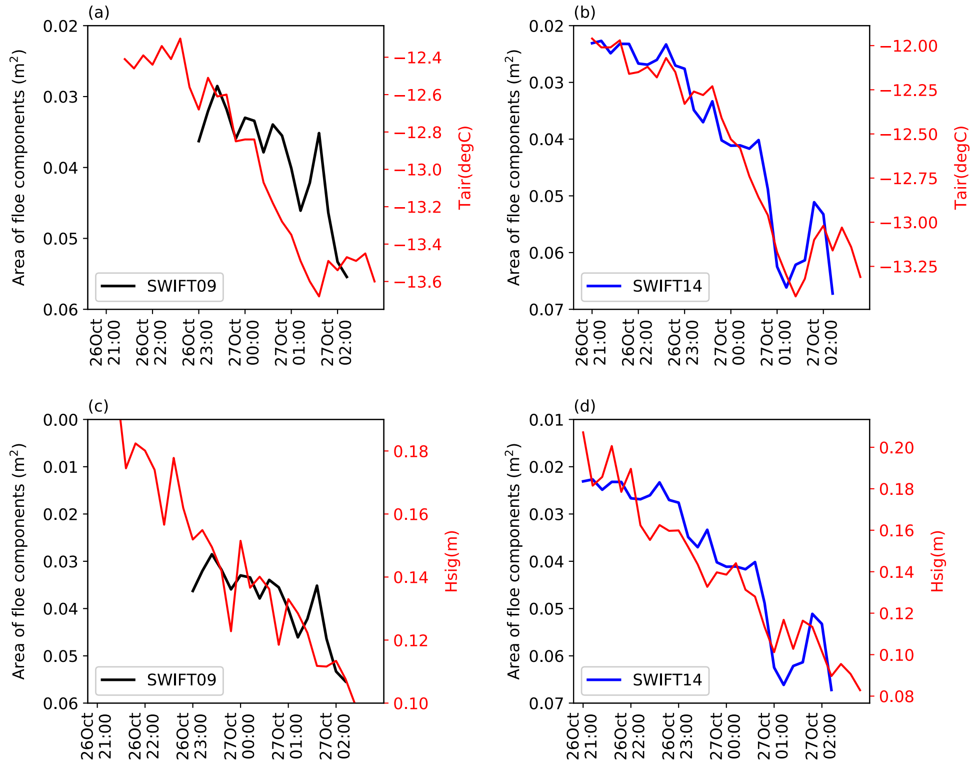

Figure 6. The evolution of the representative area of floe components over the deployment period for (a, c) SWIFT09 and (b, d) SWIFT14 shown with (a, b) air temperature (Tair) at a height of 1 m and (c, d) significant wave height (Hsig). Note that the *y* axis for floe areas is inverted for all subplots and scales differ between Figures 6a and 6b and Figures 6c and 6d to facilitate comparison with decreasing air temperature and wave heights.

the number of floe components and the number of discrete floes tells us the number of binary floe welding events that must have occurred, i.e., the the number of floe welds. The frequency of welded floes (i.e., the number of floe welds observed per number of discrete floes) increases for the whole period for SWIFT09 and between 22:00 and 01:00 UTC for SWIFT14. The frequency of welded floes is negatively correlated with significant wave height for SWIFT09 (Pearson correlation coefficient -0.71, $p < 1\%$). A positive feedback loop may be at play here: as floes get larger, they may damp waves more efficiently (Kohout & Meylan, 2008), and the resulting calmer sea state allows floes to freeze together into larger floes.

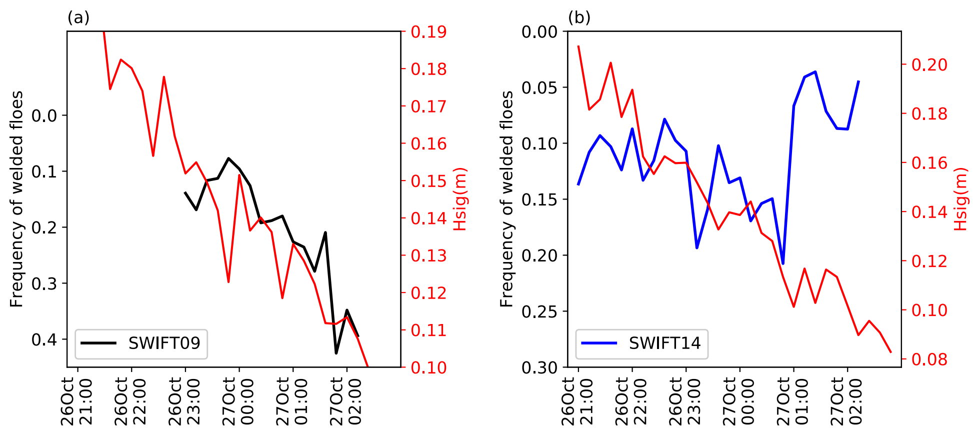

Figure 7. The frequency of welded floes (i.e., the number of floe welds observed per number of discrete floes) shown with (red axis) significant wave height over the deployment period for (a) SWIFT09 and (b) SWIFT14. Note the inverted axis for frequency of welded floes.

5. Wave Constraints on Floe Growth

Pancake sea ice floes form in the presence of surface waves, and the size of pancake floes and rate of growth depend on the wave dynamics. Prior theoretical study (Shen et al., 2001) suggested that maximum pancake size may be limited by either the tensile or bending stress mode resulting from the wave field. The tensile stress mode is caused by differential wave force which causes "stretching" of surface between floes. Thus, assuming the ice-ocean drag coefficient is negligible, floes are limited in diameter by tensile failure according to

$$D_{\max} \approx \sqrt{\frac{2C_2\lambda^2}{\pi^3 W_A g \rho_{\mathrm{ice}}}} \propto \sqrt{\frac{\lambda^2}{W_A}}. \tag{3}$$

Here λ is the wavelength, $W_A = H_s/2$ is the wave amplitude, g is gravitational acceleration, and ρ_{ice} is ice density. C_2 is the tensile stress mode parameter, which is determined by local conditions and expected to be a function of temperature and salinity. The product of C_2 with ice thickness and floe diameter, C_2Dh, is the force due to freezing between floes. Alternatively, growth of pancakes may be limited by the bending stress mode, where vertical tensile force creates bending force on floes. For bending failure, floe diameter is limited according to

$$D_{\max} \approx \frac{C_1\lambda^2}{2\pi^2 E W_A} \propto \frac{\lambda^2}{W_A}. \tag{4}$$

C_1 is a constant bending stress mode parameter, and E is the Young's modulus of the ice floe. In the laboratory, Shen et al. (2004) found that the maximum pancake size, $D_{\max}$, was proportional to the tensile stress mode rather than the bending stress mode.

Figure 8 shows equivalent floe diameter computed from the representative area of discrete floes, $\bar{A}_d$, against the tensile and bending stress mode based on wave parameters measured by SWIFTs. Wavelength is estimated from peak period using the linear finite-depth dispersion relation, solved by Newton-Raphson iteration method with depth of approximately 4,000 m. There is a strong correlation of equivalent floe diameter with both the tensile stress mode ($R^2=0.76$, $p<1\%$) and the bending stress mode ($R^2=0.74$, $p<1\%$). The linear fit in Figure 8a gives an estimate of the tensile stress mode parameter of $C_2=0.167$ kg m^{-1} s^{-2}, which is close to the estimate of $C_2=0.118$ kg m^{-1} s^{-2} observed by Shen et al. (2004) in the laboratory. We note that in their study data from both urea-doped water and saltwater (35 psu) were used.

These results indicate that waves are a dominant control on pancake ice growth, via the ratio of wavelength squared with amplitude ($\frac{\lambda^2}{W_A}$). This provides strong support for the theoretical and laboratory results of Shen et al. (2001, 2004). However, our data are not sufficient to determine which of the two mechanisms proposed in Shen et al. (2001) dominate in these field conditions.

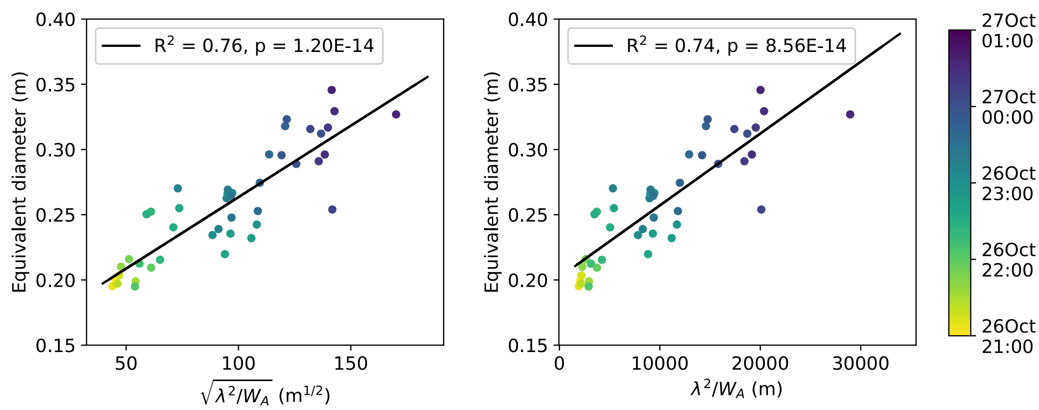

Figure 8. The equivalent diameter of discrete floes against (a) the tensile stress mode and (b) the bending mode calculated from SWIFT buoy wave measurements, with points colored by time. Regression statistics are noted in the legend. Data from both SWIFTs are included.

The representative diameter is proportional to the tensile and bending stress modes throughout the observed period of pancake ice formation (Figure 8). This is due to the feedback between the change in wave conditions with an evolving ice field. Thin ice tends to damp high frequency waves, leading to a decrease in amplitude but an increase in peak wavelength. Under the tensile and bending stress theories, these conditions correspond to larger floe sizes (Shen et al., 2004) which may contribute to more efficient damping of waves (Kohout & Meylan, 2008).

The relationship between pancake diameter and tensile and bending stress modes is expected to break down as floe diameters increase and wave amplitude decreases, and floe welding begins to take over. The good fit of the stress modes through time (Figure 8) suggests that this transition does not occur within the measurements presented here, although some welding is observed throughout the observation period.

6. Floe Welding

Roach et al. (2018b) propose that sea ice floes may merge or weld together during freezing conditions according to the geometric probability that two randomly placed floes overlap, in the absence of ocean surface waves. To describe this, they use a coagulation equation. The evolution of floe number per unit area, $\mathcal{N}$, is then proportional to concentration squared,

$$\frac{\partial \mathcal{N}}{\partial t} = -\frac{\kappa}{2}C^2, \tag{5}$$

where the rate per unit area κ is the total number of floes that weld with another, per square meter, per unit time, in the case of a fully covered ice surface ($C=1$). The square in concentration arises as the geometric probability of overlap is the product of two area fractions; see Roach et al. (2018b) for further details. Although κ may depend on surface temperature and the wave field, to implement this scheme in a large-scale model Roach et al. (2018b) assume κ is constant.

Here we calculate a value for κ, with the goodness of the linear fit showing how well the model with constant κ describes observed floe welding. By our definitions, the change in the total number of floes due to welding per unit area over some time period is simply equal to the difference between the number of components N_c and the number of discrete floes N_d (which is the number of welds) per unit area, i.e.,

$$\frac{\Delta \mathcal{N}_T^{\text{weld}}}{\Delta t} = \frac{1}{a}\frac{N_c - N_d}{\Delta t} = -\frac{\kappa}{2}C^2, \tag{6}$$

where a is the area of the image.

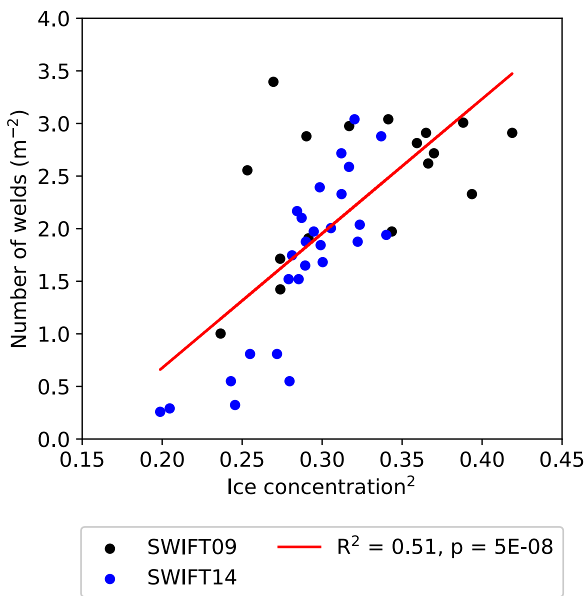

Figure 9. The number of floe welds per unit area against ice concentration squared, where the linear fit gives the coefficient of proportionality and regression statistics are noted in the legend. Data from both SWIFTs are included.

Figure 9 shows the number of welds per unit area plotted against concentration squared for each image burst. We find a linear fit to these data, with correlation coefficient $R^2=0.51$ ($p<1\%$). This provides support for the Roach et al. (2018b) floe welding model using a constant value for κ.

In a global sea ice model, κ should represent the average for various conditions. Combining data from the two buoy deployments gives an approximate fit to the two different data sets, and the slope of the fit can be used to give an approximate order-of-magnitude estimate for κ. We expect scatter in the observed relationship, as the model neglects dependence of welding on sea surface temperature and wave conditions. Although the buoys were always less than 1 km apart, they may have experienced different local conditions which influenced the welding rate, such as winds or heat fluxes.

From equation (6), the slope of the linear fit in Figure 9 is equal to $-\frac{1}{2}\kappa\Delta t$. We are unable to discern the exact time period over which welding occurred, Δt, from the images. Ship observers noted that consolidation of frazil in pancakes was visible from 21:00 UTC for SWIFT09 and from 19:00 for SWIFT14. This occurred 2 h before data from the

10.1002/2017JC013693

image processing is available. Data from the images is available over 5 h for SWIFT14 and 3 h for SWIFT09. Therefore, the maximum value that Δt could have is 7 h for SWIFT14 and 5 h for SWIFT09. Taking $\Delta t = 7$ h, we find a minimum value of $\kappa = 0.001$ m^{-2} s^{-1}. The choice of $\Delta t = 7$ h likely overestimates the time period, implying that the minimum value of κ given here is a conservative estimate. This calculation can be used to inform the parameter value choice for floe welding in future models for sea ice floe size evolution.

7. Lateral Growth of Floes

In this section, we approximately calculate what the Horvat and Tziperman (2015) model for lateral growth would predict and compare to data calculated from the SWIFT images. A more precise calculation requires a time series of sea ice thickness and net atmospheric flux at the ocean surface. Only a limited number of observations of these variables are available over our study period (Figure 5), so we assume that sea ice thickness and net atmospheric flux are constant. As we use a constant floe thickness, the notation in this section differs slightly from Horvat and Tziperman (2015).

Horvat and Tziperman (2015) suggest that a lateral growth rate can be obtained from a net flux balance, with heat fluxes near ice contributing to lateral and vertical growth of existing floes. The partitioning between the contribution of a "near-ice" heat flux, Q_{lead}, to lateral and vertical growth depends on the ratio of the basal surface areas to lateral surface areas. Let $N(r)\mathrm{d}r$ denote the number of floes per unit area with an equivalent radius between r and $r+\mathrm{d}r$. Then the area of the vertical edges of the floes, per unit ocean area, is given by

$$A_{\mathrm{lat}} = \int N(r)\frac{2h}{r}\,\mathrm{d}r = \overline{(2h/r)}, \tag{7}$$

where h is the ice thickness. The contribution of the near-ice heat flux to lateral growth, $Q_{l,l}$, is

$$Q_{l,l} = Q_{\mathrm{lead}}\left(\frac{A_{\mathrm{lat}}}{A_{\mathrm{lat}}+C}\right). \tag{8}$$

The lateral growth rate, G_r is then

$$G_r = -\frac{Q_{l,l}}{q}, \tag{9}$$

where q is the enthalpy.

The floe size distribution, $f(r)\mathrm{d}r$, is the area per unit ocean surface area covered by floes with equivalent radius between r and $r+\mathrm{d}r$. Following Horvat and Tziperman (2015), the time evolution of the floe size distribution is given by

$$\frac{\mathrm{d}f(r)}{\mathrm{d}t} = -\nabla_r \cdot [f(r)G_r] + \frac{2}{r}f(r)G_r. \tag{10}$$

Here we evolve the initially observed floe size distribution using this lateral growth scheme. Initial results indicated that using equation (8) to partition the heat flux, even with the maximum ship-based dip net measurement of sea ice thickness in equation (7), strongly underestimates the lateral growth rate. We therefore choose conditions that maximize the calculated rate, assuming that net heat flux from the ocean to the atmosphere is constant and given by the maximum ship-based estimate of net heat flux, $Q_{\mathrm{lead}} = 200$ W m^{-2} (Figure 5a). We further assume that all heat flux is used in lateral growth, $Q_{\mathrm{lead}} = Q_{l,l}$, as the dynamic conditions and thin ice suggest that heat exchange would not be limited to the space between pancakes.

We calculate an equivalent radius, r, from the areas of floe components, A_c. Floe size categories are chosen by binning all observed floe radii from both SWIFTs over the whole deployment period into 12 equally spaced categories. The initial floe size distribution, $f(r,0)\mathrm{d}r$, is the area per unit ocean surface occupied by floes of size r to $r+\mathrm{d}r$. After time Δt, the floe size distribution is

$$f(r,t)\mathrm{d}r = f(r,0)\mathrm{d}r + G_r\Delta t\left[-\frac{\mathrm{d}f(r,0)}{\mathrm{d}r} + \frac{2}{r}f(r,0)\right]\mathrm{d}r \tag{11}$$

and the evolution of the ice concentration, $C(r,t) = \int f(r,t)\mathrm{d}r$, is given by

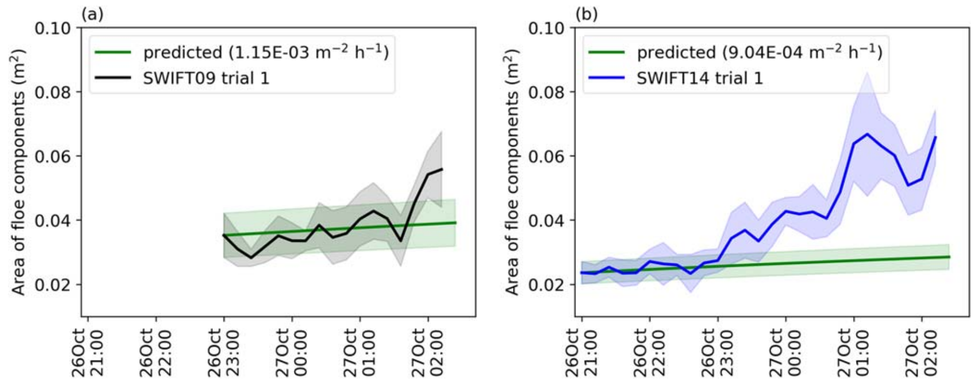

Figure 10. The representative area of floe components from SWIFT images (black), where grey shading indicates the standard deviation across subburst time variability. Also shown are the areas predicted by the Horvat and Tziperman (2015) lateral growth model, initialized from the mean properties of the first burst, with green shading indicating the evolution initialized from the range of initial conditions shown by the grey shading. The legend includes the predicted linear lateral growth rate. Both use floe areas computed in the first user trial from (a) SWIFT09 images and (b) SWIFT14 images.

$$C(r,t)=C(r,0)-G_r\Delta t\int\frac{2}{r}f(r,0)\mathrm{d}r. \tag{12}$$

These equations are evolved with $\Delta t=12$ min. The evolution of the representative floe area is given by the evolution of the total ice area divided by the initial number of floe components.

In order to sample time variability, which is the largest error source in the area observations, we repeat the calculation using initial conditions from each one of the ten images from the initial burst. We show the mean of the 10 calculations in Figure 10 using floe areas from the first user trial, with the standard deviation across the initial condition ensemble. This is compared to the observed representative area of floe components and its time variability. We find some validation for the Horvat and Tziperman (2015) model, as the value ranges from model and observations overlap for SWIFT09 and for the first 2 h of SWIFT14, but they diverge for the rest of the deployment period for SWIFT14. We are unable to conclude what conditions led the model to perform better in comparison to observations from one buoy than the other.

A constant flux is used to force the model, resulting in a linearly increasing floe area, with a rate of 1.1×10^{-3} m^2 h^{-1} for SWIFT09 and 0.9×10^{-3} m^2 h^{-1} for SWIFT14. The calculated rates are the same using floe areas from the first and second user trials (to two significant figures). A linear fit to the observed floe areas gives a lateral growth rate of 6.1×10^{-3} m^2 h^{-1} ($R^2=0.65$) for SWIFT09 and 8.6×10^{-3} m^2 h^{-1} ($R^2=0.84$) for SWIFT14. Predicted lateral growth rates are thus five and nine times smaller than those observed, in spite of our choices to maximize the lateral growth rate. However, the modeled rates are of a similar order of magnitude to observations, providing some support for the Horvat and Tziperman (2015) model.

8. Discussion

In this study, we compared observations with three theoretical models for determining floe size. The three models describe different physical processes—wave constraints on sea ice growth, floe welding, and lateral growth—all of which would be required in a comprehensive sea ice model appropriate for the marginal ice zone. Here we discuss the suitability of the models for the observed conditions and implications of this study for future work.

Very good agreement with observations of sea ice growth is found using the Shen et al. (2004) model, where stresses arising from wave force control the maximum floe size (Figure 8). The strong negative correlation of wave height with floe area (Figure 6) provides qualitative support for this model. The Shen et al. (2004) model is the only model examined here that explicitly includes wave information, and as such is best suited to the conditions observed. The relationship between pancake diameter and tensile and bending stress modes is expected to break down as floe diameters increase and wave amplitude decreases. The increase in welded floes over time observed by one SWIFT (Figure 7a) provides some indication that tensile and bending stress between floes are decreasing, such that floes can merge together. However, we do not see a transition from floe size being determined principally from wave activity to being determined by lateral welding of pancakes in the measurements presented here. Determining when this transition occurs could be useful for floe size evolution in future wave-ice coupled models. This would require observation into more quiescent wave conditions. It is worth nothing that the Shen et al. (2004) model may be of limited use for development of models of the sea ice floe size distribution, as it only predicts a single floe size. This model could instead be used to set the initial size of floes formed in a wave field.

Observations show good agreement with the relationship between floe welding and concentration arising from geometric probability, as proposed by Roach et al. (2018b). The observed relationship can be used to give an order-of-magnitude estimate of a key model parameter that determines the rate of floe welding and is highly relevant for sea ice evolution (Roach et al., 2018b). This study represents the first attempt to empirically quantify the floe welding rate. However, the size of floes observed is relatively small from a climate model perspective (although close to the smallest floe size category in Roach et al. (2018b)), and larger floes may exhibit different welding behavior. Additional field studies with a range of environmental conditions and floe sizes would give a better constraint on the welding parameter. We also note that the welding parameter is likely to depend on a variety of environmental factors, with relationships that may be difficult to determine from field measurements. Laboratory experiments, where different environmental variables can be controlled, would help unravel relationships with wave parameters and surface temperature.

Predictions based on the Horvat and Tziperman (2015) model, which uses ocean freezing potential to describe evolution of floe size distribution under lateral growth, show some overlap with observed floe area values, particularly for one buoy. Modeled growth rates are of the correct order of magnitude, but are smaller than those observed. This is despite the choice of variables to maximize the growth rate, with model predictions made using net atmospheric flux as the ocean freezing potential, which we assumed to be constant and to be used only for lateral growth. There are several possible explanations for the difference between observations and the model calculation. First, the Horvat and Tziperman (2015) model is designed to describe the transition from open water to solid ice, without resolving grease ice or crystal accumulation, processes which may be important on the short time scales observed in this study. Second, the flux in the model calculation was assumed constant, using a measurement taken after the formation of frazil crystals; better agreement with observations may be obtained using a time series of flux measurements. Third, it is possible that our analysis overestimates the observed lateral growth rate. Ice area estimates (e.g., Figure 1c) exclude loose frazil crystals on the edge of sea ice floes as they are not solid ice. However, if the ice thickens, there may be additional loose frazil crystals at depth. If this occurs, the edges of floes may become whiter and be counted as solid ice, thereby misrepresenting thickness growth as lateral growth. Further, we assumed that floe welding conserves ice area which, if untrue, may also introduce spurious lateral growth into the analysis. We are unable to determine whether these effects occur with the available data.

This study demonstrates a novel application of image processing, which allows us to isolate individual sea ice processes using images from a near-Lagrangian platform. The methods used here could be applied to existing sets of images of floe growth to obtain growth and welding time scales under different ice and atmospheric conditions, providing that floe size and surface characteristics were sufficiently uniform. For less uniform characteristics, as expected with older sea ice floes, a similar analysis could be applied using improved image processing techniques, and/or fully Lagrangian tracking of sea ice floes. Such future observational campaigns would greatly assist modeling efforts. We additionally encourage studies on other isolated floe-size-dependent processes, such as lateral melt, which is also poorly constrained and has a large effect on sea ice concentration (Roach et al., 2018a).

9. Conclusions

This study analyses images captured by drifting buoys, which show the evolution of small pancake floes in dynamic ocean conditions. The floes grow laterally and weld together to form composite floes, two processes which are quantified using image processing techniques. Lateral growth has a much greater contribution to floe size than welding during the study period. Both processes correlate with significant wave height, underlining the tightly coupled nature of wind, waves, and sea ice growth in the marginal ice zone.

The results describe three physical processes which are required for models describing sea ice floe size. We find that the Shen et al. (2001) model for pancake ice formation describes floe size well in these conditions.

Although they neglect wave activity and small-scale frazil processes, the Roach et al. (2018b) model for floe welding and Horvat and Tziperman (2015) model for lateral growth capture some of the observed behavior. We obtain an estimate for a constant floe welding parameter, which can be used for model development.

The observations presented here quantify freezing processes at the floe scale in situ for the first time. New developments in sea ice modeling which resolve small-scale, floe-size-dependent processes (e.g., Bennetts et al., 2017; Horvat & Tziperman, 2015; Zhang et al., 2016; Roach et al., 2018b) require such process-based observations to constrain parameters and validate results, which have significant impacts on simulated sea ice.

Acknowledgments
SWIFT observations were funded by ONR award N00014-13-1-0284. The data used are available from the Sea State collaboratory under the Data tab at www.apl.uw.edu/arcticseastate. L.R. and S.D. were funded via Marsden contract VUW-1408. The authors thank the crew of the *R/V Sikuliaq*, Alex de Klerk and Joe Talbert for SWIFT support, Stephen Ackley for suggesting use of this data set, and M. Jeffrey Mei for assistance with initial image processing. We are grateful to Hayley Shen, Jim Thomson, Chris Horvat, and two anonymous reviewers for comments on the manuscript.

References

Arntsen, A. E., Song, A. J., Perovich, D. K., & Richter-Menge, J. A. (2015). Observations of the summer breakup of an Arctic sea ice cover. *Geophysical Research Letters*, *42*, 8057–8063. https://doi.org/10.1002/2015GL065224

Bennetts, L. G., O'Farrell, S., & Uotila, P. (2017). Brief communication: Impacts of ocean-wave-induced breakup of Antarctic sea ice via thermodynamics in a stand-alone version of the CICE sea-ice model. *The Cryosphere*, *11*(3), 1035–1040. https://doi.org/10.5194/tc-11-1035-2017

Doble, M. J. (2009). Simulating pancake and frazil ice growth in the Weddell Sea: A process model from freezing to consolidation. *Journal of Geophysical Research*, *114*, C09003. https://doi.org/10.1029/2008JC004935

Doble, M. J., & Wadhams, P. (2006). Dynamical contrasts between pancake and pack ice, investigated with a drifting buoy array. *Journal of Geophysical Research*, *111*, C11S24. https://doi.org/10.1029/2005JC003320

Herbers, T. H. C., Jessen, P. F., Janssen, T. T., Colbert, D. B., & MacMahan, J. H. (2012). Observing ocean surface waves with GPS-tracked buoys. *Journal of Atmospheric and Oceanic Technology*, *29*, 944–959.

Horvat, C., & Tziperman, E. (2015). A prognostic model of the sea-ice floe size and thickness distribution. *The Cryosphere*, *9*(6), 2119–2134. https://doi.org/10.5194/tc-9-2119-2015

Horvat, C., & Tziperman, E. (2017). The evolution of scaling laws in the sea ice floe size distribution. *Journal of Geophysical Research: Oceans*, *122*, 7630–7650. https://doi.org/10.1002/2016JC012573

Hunke, E. C., Lipscomb, W. H., & Turner, A. K. (2010). Sea-ice models for climate study: Retrospective and new directions. *Journal of Glaciology*, *56*(200), 1162–1172.

Hunke, E. C., Lipscomb, W. H., Turner, A. K., Jeffery, N., & Elliott, S. (2015). *CICE: The Los Alamos Sea Ice Model Documentation and Software User's Manual Version 5.1* (Tech. Rep. LA-CC-06–012). Los Alamos, NM: Los Alamos National Laboratory.

Itseez. (2015). *Open Source Computer Vision Library*. Retrieved from https://github.com/itseez/opencv

Jones, N. (2009). Pancake ice takes over the Arctic. *Nature News*. https://doi.org/10.1038/news.2009.183

Josberger, E. G., & Martin, S. (1981). A laboratory and theoretical study of the boundary layer adjacent to a vertical melting ice wall in salt water. *Journal of Fluid Mechanics*, *111*, 439–473.

Kohout, A. L., & Meylan, M. H. (2008). An elastic plate model for wave attenuation and ice floe breaking in the marginal ice zone. *Journal of Geophysical Research*, *113*, C09016. https://doi.org/10.1029/2007JC004434

Leonard, G., Shen, H. H., & Ackley, S. F. (1998). *Dynamic growth of a pancake ice cover*. Paper presented at the Proceedings of 14th international symposium on ice: Ice in surface waters.

Lund, B., Graber, H. C., Persson, P. O. G., Smith, M., Doble, M., Thomson, J., & Wadhams, P. (2018). Arctic sea ice drift measured by shipboard marine radar. *Journal of Geophysical Research: Oceans*. https://doi.org/10.1002/2018JC013769

Maykut, G. A., & Perovich, D. K. (1987). The role of shortwave radiation in the summer decay of a sea ice cover. *Journal of Geophysical Research*, *92*(C7), 7032–7044. https://doi.org/10.1029/JC092iC07p07032

Onstott, R., Gogineni, P., Gow, A., Grenfell, T., Jezek, K., Perovich, D., et al. (1998). Electromagnetic and physical properties of sea ice formed in the presence of wave action. *IEEE Transactions on Geoscience and Remote Sensing*, *36*(5), 1764–1783. https://doi.org/10.1109/36.718644

Persson, P. O. G. (2012). Onset and end of the summer melt season over sea ice: Thermal structure and surface energy perspective from SHEBA. *Climate Dynamics*, *39*, 1349–1371.

Persson, P. O. G., Fairall, C. W., Andreas, E. L., Guest, P. S., & Perovich, D. K. (2002). Measurements near the atmospheric surface flux group tower at sheba: Near-surface conditions and surface energy budget. *Journal of Geophysical Research*, *107*(C10), 8045. https://doi.org/10.1029/2000JC000705

Roach, L. A., Dean, S. M., & Renwick, J. A. (2018a). Consistent biases in Antarctic sea ice concentration simulated by climate models. *The Cryosphere*, *12*, 365–383. https://doi.org/10.5194/tc-12-365-2018

Roach, L. A., Horvat, C., Dean, S. M., & Bitz, C. M. (2018b). An emergent sea ice floe size distribution in a global coupled ocean–sea ice model. *Journal of Geophysical Research: Ocean*. https://doi.org/2017JC013692

Rothrock, D. A., & Thorndike, A. S. (1984). Measuring the sea ice floe size distribution. *Journal of Geophysical Research*, *89*(C4), 6477–6486. https://doi.org/10.1029/JC089iC04p06477

Rottier, P. J. (1992). Floe pair interaction event rates in the marginal ice zone. *Journal of Geophysical Research*, *97*(C6), 9391–9400. https://doi.org/10.1029/92JC00152

Shen, H. H., & Ackley, S. F. (1995). Laboratory-produced pancake ice cover in a two-dimensional wave field. *Antarctic Journal of the United States*, *30*(5), 106–108.

Shen, H. H., Ackley, S. F., & Hopkins, M. A. (2001). A conceptual model for pancake-ice formation in a wave field. *Annals of Glaciology*, *33*(2), 361–367. https://doi.org/10.3189/172756401781818239

Shen, H. H., Ackley, S. F., & Yuan, Y. (2004). Limiting diameter of pancake ice. *Journal of Geophysical Research*, *109*, C12035. https://doi.org/10.1029/2003JC002123

Shen, H. H., & Ackley, S. F. A. (1991). A one-dimensional model for wave-induced ice-floe collisions. *Annals of Glaciology*, *15*(1), 87–95.

Spreen, G., Kaleschke, L., & Heygster, G. (2008). Sea ice remote sensing using AMSR-E 89-GHz channels. *Journal of Geophysical Research*, *113*, C02S03. https://doi.org/10.1029/2005JC003384

Thomson, J. (2012). Wave breaking dissipation observed with "SWIFT" drifters. *Journal of Atmospheric and Oceanic Technology*, *29*, 1866–1882.

Thomson, J., Ackley, S., Girard-Ardhuin, F., Ardhuin, F., Babanin, A., Boutin, G., et al. (2018). Overview of the Arctic Sea state and boundary layer physics program. *Journal of Geophysical Research: Oceans*, *123*. https://doi.org/10.1002/2018JC013766

Thomson, J., & Rogers, W. E. (2014). Swell and sea in the emerging Arctic Ocean. *Geophysical Research Letters*, *41*, 3136–3140. https://doi.org/10.1002/2014GL059983

Vancoppenolle, M., Fichefet, T., Goosse, H., Bouillon, S., Madec, G., & Maqueda, M. A. M. (2009). Simulating the mass balance and salinity of Arctic and Antarctic sea ice. 1. Model description and validation. *Ocean Modelling*, *27*(1–2), 33–53. https://doi.org/10.1016/j.ocemod.2008.10.005

Wadhams, P., Aulicino, Parmiggiani, G. F., Persson, P. O. G., & Holt, B. (2018). Pancake ice thickness mapping in the Beaufort Sea from wave dispersion observed in SAR imagery. *Journal of Geophysical Research: Oceans*, *123*. https://doi.org/10.1002/2017JC013003

Wadhams, P., Lange, M., & Ackley, S. F. (1987). The ice thickness distribution across the Atlantic sector of the Antarctic Ocean in midwinter. *Journal of Geophysical Research*, *92*(C13), 14535–14552. https://doi.org/10.1029/JC092iC13p14535

Weeks, W. F. S., & Ackley, S. F. (1986). The growth, structure, and properties of sea ice. In N. Untersteiner (Ed.), *The geophysics of sea ice* (Vol. 146, pp. 9–164). Berlin, Germany: Springer. https://doi.org/10.1002/9781444317145.ch2

Zhang, J., Schweiger, A., Steele, M., & Stern, H. (2015). Sea ice floe size distribution in the marginal ice zone: Theory and numerical experiments. *Journal of Geophysical Research: Oceans*, *120*, 3484–3498. https://doi.org/10.1002/2015JC010770

Zhang, J., Stern, H., Hwang, B., Schweiger, A., Steele, M., Stark, M., et al. (2016). Modeling the seasonal evolution of the Arctic sea ice floe size distribution. *Elementa: Science of the Anthropocene*, *4*(1), 126. https://doi.org/10.12952/journal.elementa.000126